arXiv:1907.08065v1 [cs.RO] 18 Jul 2019

Design and Take-Off Flight of a Samara-Inspired Revolving-Wing Robot

Songnan Bai and Pakpong Chirarattananon

***Abstract*— Motivated by a winged seed, which takes advantage of a wing with high angles of attack and its associated leading-edge vortex to boost lift, we propose a powered 13.8-gram aerial robot with the maximum take-off weight of 310 mN (31.6 gram) or thrust-to-weight ratio of 2.3. The robot, consisting of two airfoils and two horizontally directed motor-driven propellers, revolves around its vertical axis to hover. To amplify the thrust production while retaining a minimal weight, we develop an optimization framework for the robot and airfoil geometries. The analysis integrates quasi-steady aerodynamic models for the airfoils and the propellers with the motor model. We fabricated the robots according to the optimized design. The prototypes are experimentally tested. The revolving-wing robot produces approximately 50% higher lift compared to conventional multirotor designs. Finally, an uncontrolled hovering flight is presented.**

I. Introduction

Micro Aerial Vehicles (MAVs) have gained an increasing popularity thanks to their countless applications, such as agricultural, inspection, and reconnaissance. With an ability to hover and the exceptional maneuverability, rotary-wing vehicles, in particular, prove to be a highly versatile platform. At small scales, however, flying robots suffer from limited flight endurance due to the increased dominance of viscous forces [1]. Compared to the fixed-wing counterparts, rotorcraft are less efficient. The absence of large aerodynamic surfaces in rotary-wing designs comes with an inevitable expense of the energetic efficiency.

To date, nature has provided us solutions for recreation of flight with man-made machines. Bird-like morphing wings manifest high performance aerodynamic surfaces [2]. Taking after insects and hummingbirds, millimeter-scale flying robots leverage unsteady force production and leading-edge vortices as a lift enhancement mechanism through the flapping-wing motion [1], [3]. In this work, we take an inspiration from winged achenes or autorotating seeds and propose a revolving-wing robot that is capable of hovering with a promising aerodynamic performance.

Similar to insect wings, a samara operates at low Reynolds numbers and high angles of attack in comparison to conventional aircraft wings or propeller blades. At small Reynolds numbers, large wing pitch angles result in an improved aerodynamics performance [4]. During descent, a maple seed autorotates into a helical fall and exhibits elevated lift as a result of a stably attached leading-edge vortex [5], [6]. Herein, we translate these principles into a powered rotating robot in figure 1, exploiting two revolving flat airfoils with high angles of attack for thrust generation.

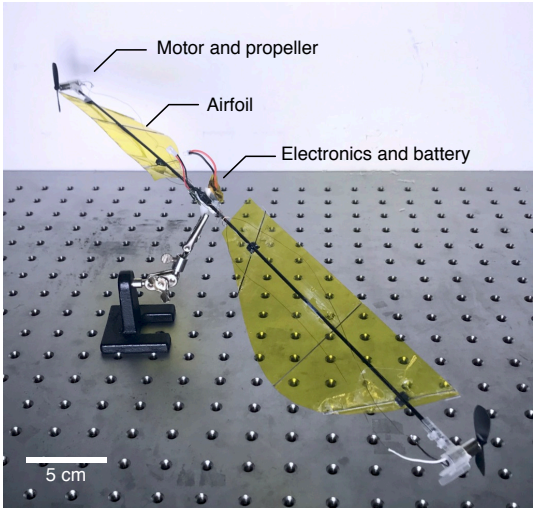

Fig. 1. Photograph of a flight-capable samara-inspired robot with two large aerodynamic surfaces. The mass of the motor-driven robot is 13.8 gram.

Unlike monocopters [7], which rely solely on propeller's thrust to stay aloft, robotic samaras resort to rotating airfoils, relegating the role of propellers such that they are predominantly for countering the aerodynamic drag produced by the airfoils. This is akin to the function of propellers on fixed-wing aircraft. In [8], powered flights of two robotic samaras with masses of 75 g and 38 g have been demonstrated. The robots incorporate a monowing design that takes after natural samaras. Due to the sophisticated aerodynamics and flight trajectories, the authors carried out over 100 iterations to reach the two final designs that have the lift-to-weight ratios of 1.67 and 1.36. Another related robot is presented as a 532-gram hybrid robot with a 105-cm wingspan [9].

Unlike previous revolving robots, our proposed samara-inspired robot adopts a symmetric dual-wing design with horizontally directed propellers. The symmetric design simplifies the modeling efforts, resulting in more tractable dynamic and aerodynamic models. In this configuration, the vertical thrust is solely contributed by two wings. To create a lightweight vehicle that hovers efficiently, we borrow fabrication and aerodynamic modeling techniques from both flapping-wing robots [1], [3] and rotary-wing aircraft [10]. Employing momentum theory (MT) and blade element method (BEM), the aerodynamics of airfoils are modeled according to the wing profile [11]. To further promote payload capacity and the thrust-to-weight ratio, we take into account

This work was substantially supported by the Research Grants Council of the Hong Kong Special Administrative Region of China (grant number CityU-11207718).

The authors are with the Department of Biomedical Engineering, City University of Hong Kong, Hong Kong SAR, China (emails: songnabai2-c@my.cityu.edu.hk and pakpong.c@cityu.edu.hk).

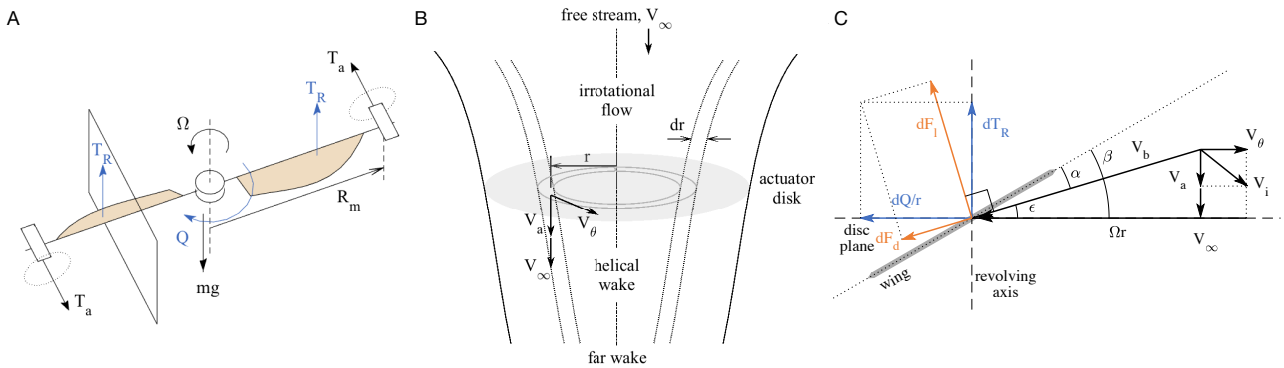

Fig. 2. (A) A free body diagram illustrating the dynamics of the robot in a revolving flight. (B) Streamtube and annular element for the momentum theory. The induced velocity is presented as the axial and tangential velocities. (C) Forces and relative airflow velocities experienced by a wing element as seen from a cross section shown in (A).

the actuators' dynamics. Since the performance of the motors and propellers on the robot is affected by the revolving motion because the translating motion of the propeller, which substantially depends on the revolving rate of the robot, influences the propeller's thrust, this impacts the ability of the propellers to overcome the aerodynamic drag produced by the airfoils. By taking into account the aerodynamics of the airfoils, the propellers, and steady-state motor model simultaneously, we present a framework for determining the optimal geometry of the robot. The performance of the fabricated robots is empirically examined against the model predictions. Finally, we demonstrate a passively-stable open-loop flight of the robot with the optimal design.

II. Robot Dynamics

A. Overview

The proposed robot, schematically depicted in figure 2A, takes an inspiration from a winged seed or a samara. Vertical thrust is produced by two large, revolving aerodynamic surfaces—airfoils. Two motor-driven propellers are horizontally aligned in the opposite directions. The propellers' thrusts make no direct contribution to the robot's vertical thrust, and are solely for producing a rotational torque in order to counter the torque created by the aerodynamic drag from the revolving wings.

To simplify the analysis, we consider first the dynamics of the airfoils and then, the dynamics of the motor-driven propellers, neglecting the possible flow interaction. In section II-B, we employ classical momentum theory (MT) and blade element method (BEM) to demonstrate that when the robot revolves at the angular rate Ω, the thrust generated by each airfoil (T_R), and the associated drag torque (Q) about the yaw axis of the robot follows

$$T_R = C_{T,R}\Omega^2 \quad \text{and} \quad Q = C_Q\Omega^2, \tag{1}$$

where $C_{T,R}$ and C_Q are the corresponding thrust and torque coefficients that can be evaluated according to the geometry of the airfoils.

For actuation, the complication arises as the propellers, placed at distance R_m from the revolving axis (see figure 2A), have non-zero translational velocities. In section II-C, we show that the thrust generated by each motor-driven propeller (T_a) depends not only on its driving voltage (U), but also on its axial speed (ΩR_m). In other words, the dynamics of the propellers are influenced by the robot's revolving rate. In equilibrium, or the hovering condition, the yaw torque resulted from the aerodynamic drag from the airfoils must be balanced by the yaw torque contributed by the thrusts generated by the propellers: $Q = T_a R_m$.

B. Airfoil Aerodynamics

To analyze the aerodynamics of the airfoils, we employ MT and BEM. MT assumes the conservation of mass and momentum to relate the thrust and aerodynamic drag torque of the propeller with the induced air velocity. On the other hand, BEM exploits the quasi-steady assumption to provide the aerodynamic forces as functions of the local air speed. Together, the aerodynamic forces are evaluated according to the revolving speed of the airfoil and its geometry.

1) Momentum theory: Momentum theory regards spinning propellers or revolving airfoils as an infinitesimally thin actuator disc. The airflow is confined within the boundaries of an axisymmetric streamtube as shown in figure 2B. The conservation of mass imposes a constant flow rate throughout. The downwards free-steam velocity (V_∞) represents the upstream air velocity distant from the disc. The actuator disc produces the thrust in the form of a pressure discontinuity immediately above and below the disc. Simultaneously, it introduces the additional air velocity, known as the induced velocity $\mathbf{V}_i(r)$, to the wake. This induced velocity is assumed to vary as a function of the radial position (r). Due to the rotational motion of the airfoils, the induced velocity is a vector sum of the axial flow ($V_a(r)$) and the tangential flow ($V_\theta(r)$).

To compute the thrust generated by the actuator disc, one considers an annular element of the flow with the radius r and width $\mathrm{d}r$. As given in [12], [13], the elemental thrust $\mathrm{d}T_R$ is obtained using the conservation of momentum along the axial direction as

$$\mathrm{d}T_R(r) = 4\pi r\rho\left(V_\infty + V_a(r)\right)V_a(r)\,\mathrm{d}r, \tag{2}$$

where $\rho = 1.2$ kg.m^{-3} is the air density. Likewise, the conservation of angular momentum relates the tangential induced velocity V_θ to the elemental torque $\mathrm{d}Q$ on the airfoils [12], [13]:

$$\mathrm{d}Q\left(r\right) = 4\pi r^2 \rho \left(V_\infty + V_a\left(r\right)\right) V_\theta\left(r\right) \mathrm{d}r. \tag{3}$$

If we restrict our analysis to a hovering robot, the free-steam velocity associated to the airfoils is zero. Equations (2) and (3) reduce to

$$\mathrm{d}T_R\left(r\right) = 4\pi r \rho V_a^2\left(r\right) \mathrm{d}r, \tag{4}$$

$$\mathrm{d}Q\left(r\right) = 4\pi r^2 \rho V_\theta\left(r\right) V_a\left(r\right) \mathrm{d}r. \tag{5}$$

That is, MT provides the expressions of robot's thrust and the drag torque in terms of the induced velocity.

2) Blade element method: Blade element theory considers aerodynamics forces based on the airfoil's geometry. For a flat wing, the geometry of an airfoil is specified by the wing pitch angle (β) the chord function ($c\left(r\right)$). BEM radially divides the airfoil into multiple elements described by r and $\mathrm{d}r$. Total aerodynamic force or torque is evaluated as a contribution of all elements.

Consider a hovering robot, its wing element at the radial position r has a translational velocity Ωr relative to the inertial frame. According to MT above, the local airspeed is given by the induced velocity ($\mathbf{V}_i$). As a result, the respective wing element experiences the perceived airspeed (V_b) of

$$V_b = \sqrt{\left(\Omega r - V_\theta\right)^2 + V_a^2}, \tag{6}$$

as illustrated in figure 2C. The BEM states that the lift F_l and drag F_d forces on the wing element are proportional to aerodynamic pressure and the associated lift and drag coefficients ($C_l\left(\alpha\right)$ and $C_d\left(\alpha\right)$), such that $\mathrm{d}F_{l,d}\left(r,\alpha\right) = \frac{1}{2}\rho V_b^2\left(r\right) C_{l,d}\left(\alpha\right) c\left(r\right) \mathrm{d}r$, where the angle of attack (α) describes the orientation of the airfoil relative to the air flow. Lift ($\mathrm{d}F_l$) and drag ($\mathrm{d}F_d$) act in perpendicular and parallel to $V_b\left(r\right)$. To obtain the thrust and drag torque, elemental lift and drag are projected on to the vertical and horizontal directions. This yields

$$\mathrm{d}T_R\left(r\right) = N\left(\mathrm{d}F_l\left(r,\alpha\right)\cos\epsilon - \mathrm{d}F_d\left(r,\alpha\right)\sin\epsilon\right), \tag{7}$$

$$\mathrm{d}Q\left(r\right) = Nr\left(\mathrm{d}F_l\left(r,\alpha\right)\sin\epsilon + \mathrm{d}F_d\left(r,\alpha\right)\cos\epsilon\right), \tag{8}$$

where $N = 2$ is the number of airfoils. The angle of attack (α) and the blade downwash angle (ϵ) can be found from figure 2C as

$$\epsilon = \tan^{-1}\left(\frac{V_a}{V_\theta - \Omega r}\right) \quad \text{and} \quad \alpha = \beta - \epsilon.$$

To compute the thrust and torque coefficients (equation (1)) of the robot, we consolidate the outcomes from MT and BEM. Equations (4)-(5) are incorporated with (7)-(8) to eliminate the axial and tangential velocities. The elemental thrust and torque are then integrated over the whole wing to yield the total thrust and torque. The resultant thrust and torque coefficients can be numerically computed according to the wing chord profile ($c\left(r\right)$) and the pitch angle (β).

C. Propellers' Dynamics

In our design, the propellers, driven by DC motors, are responsible for generating the torque to counter the aerodynamic drag from the airfoils. The revolving design requires the propellers to traverse with respect to the inertial frame in flight. As a consequence, in addition to the driving voltage, the aerodynamic forces produced by the propellers depend on the revolving speed of the robot. In order to determine the propeller's thrust, both the dynamics of the propeller and the motor must be considered together.

1) Propeller aerodynamics: Similar to the airfoils, the aerodynamics of the propellers can be modeled with MT and BEM, with some modifications. In the hovering condition, the translational speed of the propeller depends on its distance from the revolving axis (R_m) and the revolving rate as ΩR_m (not to be confused with the spinning rate of the propeller, ω). From MT, this constitutes an axial free stream velocity of the air seen by the propeller. In addition, if the tangential induced velocity is neglected as in [10], the axial induced velocity (v_i) is independent of the radial position. The thrust generated by the propeller (T_p) according to MT takes the form resembling the integration of equation (2):

$$T_p = 2\rho\pi R_p^2 v_i\left(v_i + \Omega R_m\right), \tag{9}$$

where R_p is the propeller's radius. Using the same framework as the airfoils, it has been shown in [10] that BEM provides an expression for the thrust of an n-blade propeller with radius R_p as

$$T_p = \frac{1}{2}\rho n R_p^4 \left(a_0 - a_1 \frac{v_i + \Omega R_m}{\omega R}\right)\omega^2, \tag{10}$$

where a_0 and a_1 are dimensionless lumped coefficients related to the propeller's pitch and chord profiles. This equation assumes the propeller blade has constant pitch and chord, and infinite aspect ratio [10]. While this is not the case for our propellers, we believe the model still captures the dominant aerodynamic effects. Relaxation of these assumptions primarily leads to different definitions of the lumped parameters. Under the same assumption, the propeller's torque due to the aerodynamic drag is given by

$$\tau_p = \frac{1}{2}\rho n R_p^5 a_2 \omega^2 + \left(T_p \frac{\kappa v_i + \Omega R_m}{\omega}\right), \tag{11}$$

where a_2 is another dimensionless lumped parameter for the blades, and κ is the induced power factor which accounts for the power loss caused by wake rotation and tip loss. Unlike standard airfoils, lumped coefficients and the power factor for propellers are commonly empirically determined [10].

We solve for the induced velocity as a function of Ω and ω by combining the result from MT (equation (9)) and BEM (equation (10)). It follows that the propeller's torque can be numerically evaluated for each Ω and ω pair as long as the lumped coefficients are known.

2) First-order motor model: In this part, we employ a first-order model to relate the motor's driving voltage, output torque, and the rotational rate. For a motor-driven propeller,

this directly links the driving voltage (U) to the propeller's torque (τ_p) and spinning speed (ω).

In steady state, where the rotational rate is constant, the voltage law states $U = IR_i + k\omega$, where, I denotes the current, R_i is the motor's internal resistance, and the $k\omega$ term represents the back EMF, assumed proportional to ω with a motor constant k. The motor torque is given as $\tau_p = kI$. Hence,

$$\tau_p = \frac{k}{R_i}\left(U - k\omega\right). \tag{12}$$

D. Integrated robot dynamics

With the aerodynamics and actuator's dynamics of the propeller analyzed, we consolidate the findings to yield an integrated model. When combined, equations (11) and (12) enable us to determine ω as a function of U and Ω. With the expression of propeller's thrust (equation (10)), we get rid of ω and obtain a direct relationship between T_p, U, and Ω as $T_p = T_p\left(U, \Omega\right)$. Next, in the hovering condition, the robot's yaw torque contributed by the propellers balances out the airfoil drags (equations (1)), such that $2R_m T_p\left(U, \Omega\right) = Q\left(\Omega\right)$. Finally, we find the vehicle's revolving speed for a particular motors' driving voltage. This, when substituted back into equation (1), we obtain a prediction of the robot's thrust given the input voltage. The framework enables us to estimate the generated thrust from the robot and airfoil geometries.

III. Design Optimization

In the previous section, we investigate the dynamics of the robot. The framework enables us to predict the total thrust generated by the robot, given the voltage supplied to the actuators. The results depend on relevant parameters related to aerodynamics, airfoil geometry, and motors. In this section, we identify these model parameters and search for the optimal wing geometry for maximizing the robot's thrust based on the set of chosen hardware.

A. Model Parameters

In the airfoil model, the relevant aerodynamic parameters used for BEM are lift and drag coefficients, C_l and C_d. Both of them depend on the angle of attack α. Since the airfoils of our prototype are flat and operate at large angles of attack with low to intermediate Reynolds numbers ($\sim 2.5 \times 10^4$). The conditions are similar to those of large insect wings [5], [14]. Several quasi-steady aerodynamic studies [12], [14], [15] have established approximate forms of lift and drag coefficients for BEM as

$$C_l\left(\alpha\right) = C_{l,1}\sin\left(2\alpha\right), \tag{13}$$

$$C_d\left(\alpha\right) = C_{d,0} + C_{d,1}\left(1 - \cos\left(2\alpha\right)\right), \tag{14}$$

where the coefficients $C_{l,1}$, $C_{d,0}$, $C_{d,1}$ are typically empirically determined. Equations (13) and (14) also resemble the results from the flat plate theory used for small gliders [16]. Without prior experimental data, we approximate these coefficients from related literature as $C_{l,1} = 1.72$, $C_{d,0} = 0.11$, and $C_{d,1} = 1.94$ [17].

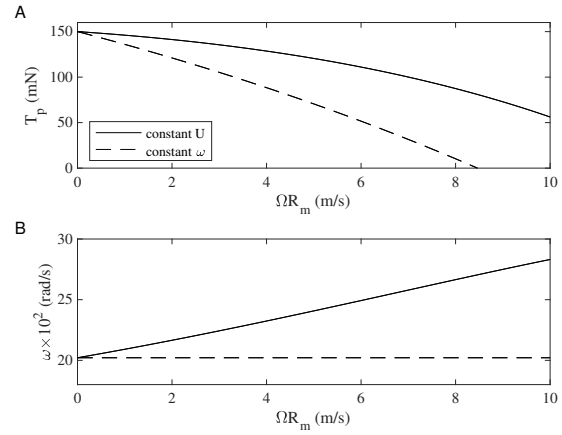

Fig. 3. The propeller's thrust (A) and spinning speed (B) plotted against the axial inflow speed. The solid lines indicate the results from the model, assuming a constant driving voltage of 3.5 V. The dashed lines show the thrust prediction in the scenario where ω is held constant..

For the motors and propellers, our prototype uses coreless DC motors and matched propellers from Crazyflie 2.0. The motor parameters of $R_i = 1.58\ \Omega$ and $k = 1.1$ mV·s·rad^{-1} are taken from previous identification results in [18]. Similarly, the associated blade coefficients and power factor have been given in [18] as $a_0 = 0.3633$, $a_1 = 1.9960$, $a_2 = 0.0022$, and $\kappa = 1.87$. The maximum supplied voltage is conservatively chosen to be 3.5 V.

With the listed parameters, figure 3 shows the model predictions of the propeller's thrust and its rotational rate against the linear axial speed (ΩR_m) as outlined in Section II-C. The plots reveal that, assuming a constant voltage $U = 3.5$ V, the generated thrust drops, whereas the propeller's speed (ω) increases, as the revolving rate (Ω) rises. This is because the axial velocity effectively reduces the aerodynamic drag seen by the propeller. For comparison, we plot the thrust prediction in case ω remains constant. In such case, the model severely underestimates the propeller's thrust at high axial velocity. This verifies that it is essential to take into account the revolving rate of the robot when analyzing the propeller's dynamics.

B. Optimization Method

With the proposed dynamic models and associated parameters, we proceed to search for the optimal airfoil design and propellers' placement. The optimization problem is setup as

$$\mathbf{x}^* = \max_{\mathbf{x}} T_R\left(\mathbf{x}\right) - m\left(\mathbf{x}\right)g, \tag{15}$$

subject to some chosen constraints, where $\mathbf{x} \in R^6$ is a set of variables to be optimized, $m\left(\mathbf{x}\right)$ is the mass of the robot, and g is the standard gravity. The proposed objective function, unlike the thrust-to-weight ratio, is intended for maximizing the payload capability of the robot.

Here, we use six design variables: wing pitch angle β, position of the propellers R_m, wing semi-span R_{tip}, and three parametrized chord lengths $c_1 - c_3$. We impose the wing root position to be at $0.15R_{tip}$. Restricting the wing's

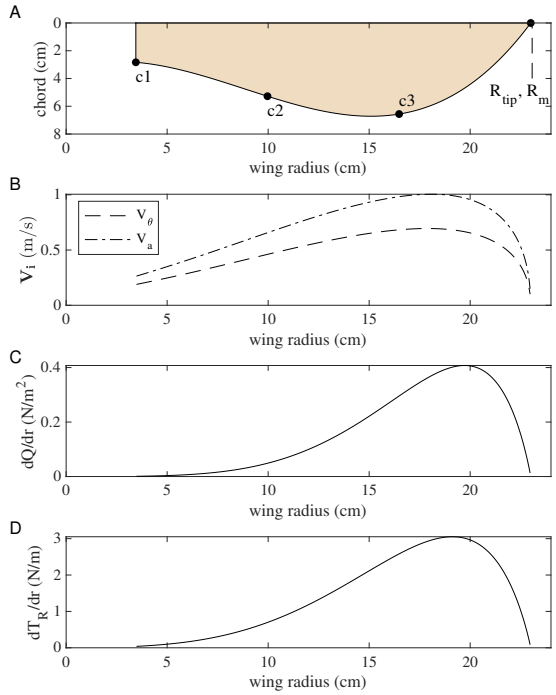

Fig. 4. (A) The optimal wing geometry and location of the motor. The corresponding wing pitch angle is $27.5°$ (not shown). (B) The induced axial and tangential velocities at different points along the wing, assuming the robot revolves at the speed corresponding to $U = 3.5$ V. (C) Distribution of the drag torque. (D) Distribution of the airfoil's thrust.

leading edge to a straight line, the variable c_1 corresponds to the length of the chord at the wing's root, whereas c_2 and c_3 are the chord lengths at two intermediate locations uniformly separated between the wing's root and the wing's tip as illustrated in figure 4A. Assuming other components are unchanged, $m(\mathbf{x})$ is taken as the mass of the airframe and of the wings, calculated using the linear density of the airframe (carbon fiber rod) of 4.7 g·m^{-1} and the areal density of the wings (polyamide film and wing spars) of 92.6 g·m^{-2}. In addition, we incorporate the following constraints.

- We limit $R_m \geq R_{tip}$ for the ease of fabrication, such that the motors and propellers can be physically mounted without interfering with the wings.
- The maximum semi-span is selected to avoid undesirably large prototypes, such that $R_{tip} \leq 23$ cm. This is because MT favors a larger actuator disc as it requires lower power for thrust generation [10].
- The chord length at the wing tip is zero. The unmodeled tip loss effects demote the airfoil efficiency thanks to tip vortices [10], rendering the airfoil aerodynamically inefficient near the tip.

The final wing profile is computed from a cubic spline interpolation of optimized variables.

C. Optimal Airfoils

The proposed optimization problem is solved with the Nelder–Mead simplex algorithm. While this does not guarantee a globally optimal solution, we achieve a local solution with the predicted thrust of 285 mN. The corresponding robot profile is drawn in Figure 4A, with the wing pitch angle of $27.5°$. The optimized wing design has a relatively narrow width near the root, with the largest chord near the location of c_3. Figure 4B-D also shows the predicted induced velocities and aerodynamic pressure at locations along the airfoil.

The plot of induced velocities reveal that the induced airflow is markedly slower than the translational speed ($\sim \Omega R_m$), which can be as large as $\approx 5 - 10$ m·s^{-1}. Equations (6) and (7), therefore, suggest that the thrust is majorly contributed by the wing's translation. As a consequence, the optimal wing features a wider chord further away from the revolving axis, leading to the elemental thrust and torque in Figure 4C and D that peak near the wing tip. In the meantime, while the wing area near the root gives rise to relatively little thrust, the chord length at the wing root is still notable. This is because closer to the revolving axis, this area favorably contributes less towards the drag torque.

IV. Experimental Validation

A. Fabrication and Components

The robot consists of four primary components: the airframe, airfoils, a pair of motors and propellers, and flight electronics, as shown in figure 1.

The airframe was constructed from a carbon fiber rod with 2-mm diameter. The airfoils, or wings, were made from 250-μm polyimide film (Kapton), laser cut to the desired geometry using CO_2 laser (Epilog Mini 24). The wings remain flat in flight thanks to the structural support provided by the wing spars (carbon fiber rod with 0.5-mm diameter). The wings are attached to the airframe via small 3D printed parts (Black resin, Form 2, Formlabs). The design of these printed parts dictates the wing pitch angle. All parts are fixed together using Cyanoacrylate adhesives and epoxy resin.

For actuation, we employed 23-mm radius propellers and 7×16-mm coreless DC motors commercially available as parts for Crazyflie 2.0 for the prototypes. According to the measurements in [18], each propeller can generate $\approx 90 - 180$ mN when the motor is supplied by the voltage 2.5-4.0 V. The motors were driven by a micro 2.4GHz RC servo receiver with two built-in Electronic Speed Controllers (Deltang DT Rx31d). A single-cell 100-mAh Li-ion battery was for power. The mass of the robot is 13.8 g.

For validation of the optimized design, we fabricated four robots for comparison, robot Ⓐ with the optimal wing geometry and wing pitch angle ($27.5°$); robot Ⓑ with the same wing geometry, but with the wing pitch angle of $11.0°$; robot Ⓒ with the same wing geometry, but with the wing pitch angle of $40.0°$; and robot Ⓓ with the same planform area and winspan, but with a constant chord and the wing pitch angle of $21.0°$. All robots weigh approximately the same as they all carry identical parts and wing areas.

B. Force Measurements

1) Experimental Setup: To evaluate the thrust generated by the robots, we perform static experiments to measure the generated force when the robots were given various commands. The experimental setup is schematically presented

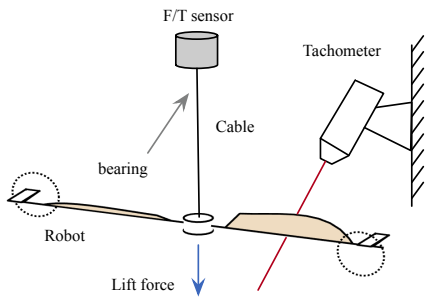

Fig. 5. Experimental setup for measurements of the revolving speed and generated thrust.

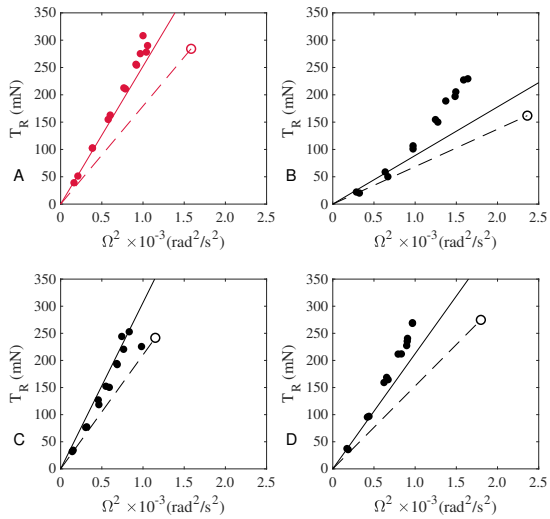

Fig. 6. The thrust and revolving speed measurements from four prototypes (dots). The dashed lines show the model predictions based on the used coefficients, with hollow circular points representing the expected maximum thrust when the motors are driven at $U = 3.5$ V. The solid lines indicate the refitted model predictions with the revised lift and drag coefficients. (A) corresponds to the robot the optimal airfoils and the optimal wing pitch angle of $27.5°$; (B) with the wing pitch angle of $11°$; (C) with the wing pitch angle of $40°$; and (D) with the rectangular wings and the wing pitch angle of $21°$.

in figure 5. The robot was suspended upside down from the load cell (Nano17, ATI) by a cable. The rated sensor resolution of 3.1 mN is notably lower than the expected thrust. A rolling bearing was incorporated proximal to the load cell to allow the robot and the cable to freely rotate. The load cell was covered for thermal insulation to eliminate a possible convective effects due to the wake generated by the robot. A tachometer (Advent A2108) was mounted above the robot for measuring the revolving speed.

In this configuration, the generated thrust force directs downward and can be measured by the sensor through the cable. Thanks to the symmetry, during operation, the robot retained an approximate upright orientation. The thrust is assumed vertical, or aligned with the sensor's primary axis. The weight of the robot and other parts can be directly subtracted from the measurements to obtain the thrust.

2) Measurement Results: We performed the experiments on four robots with different configurations as presented in Section (IV-A). For each trial, we recorded the thrust, averaged from 10 s, when the revolving speed was approximately constant. We remotely commanded seven different voltage setpoints. Both motors on the robot received an identical voltage. Two measurements were obtained for each setpoint. In total, we acquired 14 datapoints for each robot, or 56 datapoints among four robots. In all datapoints, the cycle averaged horizontal force is less than 5% of the vertical component.

Due to the lack of onboard measurements, we are unable to record the actual voltage of the motors. Figure 6 demonstrates the measured thrusts against the squared revolving speed. Apart from robot Ⓑ (figure 6B), which has relatively low wing pitch angle, the outcomes follow an approximately linear trend as predicted by equation (1).

The measurements, as anticipated, verify that robot Ⓐ, with the optimized design, generates the thrust up to 310 mN, equating to the thrust-to-weight ratio of 2.3 (Figure 6A). This number markedly reduces to ≈ 250 mN for robots Ⓑ and Ⓒ. Robot Ⓓ, on the other hand, has the maximum thrust of 270 mN , approximately 10% lower than that of robot Ⓐ. For comparison, we separately measured the maximum thrust force generated by a vertically-aligned motor-propeller pair with no revolving wings using the same driving board and battery. The force produced by two propellers is 207 mN, significantly lower than all four revolving-wing robot prototypes. In particular, with respect to robot Ⓐ, the revolving-wing configuration amplifies the lift by approximately 50% (from 207 to 310 mN). The results highlight the benefit of the proposed samara-inspired design.

Figure 6 also shows the thrust predictions according to equation (1) based on the parameters given in Section (IV-B.2) in dashed lines. The unfilled circular points indicate the predicted thrust when $U \approx 3.5$ V. While the general trends are in agreement with the experimental data, the model consistently underpredicts the generated thrusts and overpredicts the revolving speeds. We believe these are primarily due to the inaccuracy of both aerodynamic parameters (such as $C_l(\alpha)$ and $C_d(\alpha)$, $a_i's$, κ, etc.) and motor parameters (including R_i and k), owing to the lack of prior experimental data.

In an attempt to ameliorate the model's accuracy. We revise the aerodynamic parameters $C_{l,1}$, $C_{d,0}$ and $C_{d,1}$ by finding a new set of parameters that minimize the root mean square errors of the thrust predictions from equation (1) using all 56 data points. In figure 6, the solid lines present the refitted thrust predictions with $C_{l,1} = 2.67$, $C_{d,0} = 0.22$ and $C_{d,1} = 2.58$. Without direct measurements of U, T_p or Q, we are unable to revise other model parameters. This leaves room for improvement in the future.

C. Lift-off Flight

The static tests suggest that the prototype with the optimal design (robot Ⓐ) is capable of producing sufficient thrust for flight. In the current prototypes, without an onboard flight controller, we are unable to implement real-time feedback control. Nevertheless, a revolving-wing robot possesses passive attitude stability as long as certain conditions related to the inertial tensor are satisfied [8].

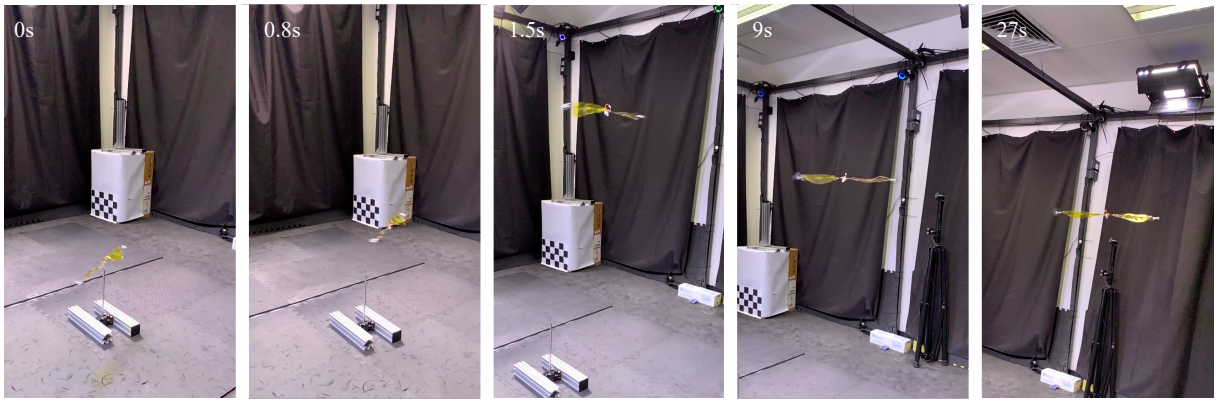

Fig. 7. Frames at various times during the robot's flight. The first three frames show the take off of the robot. The latter two give its normal flight.

To demonstrate a flight, the robot was placed on a launch platform that allows the robot to revolve and gain sufficient rotational speed before lifting off. The robot was remotely controlled for propellers' thrust as an indirect way to regulate its altitude manually by a human operator. Figure 7 displays the video frames of the robot during the takeoff and up to 27 s after. At the beginning, the robot climbed over 1.5 m in less than two seconds. During the flight, we observed minimal lateral drift. Correspondingly, the tip-path plane remained relatively horizontal during the whole flight.

V. Conclusion

Motivated by flight of a winged achene, in this work, we have proposed a modeling framework for a motor-driven revolving-wing robot. Exploiting the devised dynamic models, we fabricated a 13.8-gram robot with an optimal design and demonstrated a hovering flight. The developed framework entails uses of quasi-steady aerodynamic methods, namely momentum theory and blade element method, for describing the dynamics of the airfoils and propellers. The actuation system (motors and propellers) was taken into account in the airfoil design in an attempt to maximum the thrust generated by the robot. Based on the design optimization, the manufactured robot has the maximum take-off weight of 310 mN and thrust-to-weight ratio of 2.3. The revolving airfoils boost the thrust by $\approx$50% compared to multirotor designs. In a flight demonstration, the robot displayed a stable hovering flight without active stabilization.

In the future, we plan to perform extensive measurements on both airfoils and the actuation system for parameter identification in order to improve the model accuracy. Further improvements can be achieved by taking into consideration the aerodynamic interaction between the airfoils and the propellers. To achieve position controlled flight, flight dynamics must be extensively studied.

References

[1] Y. Chen, H. Wang, E. F. Helbling, N. T. Jafferis, R. Zufferey, A. Ong, K. Ma, N. Gravish, P. Chirarattananon, M. Kovac *et al.*, "A biologically inspired, flapping-wing, hybrid aerial-aquatic microrobot," *Science Robotics*, vol. 2, no. 11, p. eaao5619, 2017.

[2] B. Jenett, S. Calisch, D. Cellucci, N. Cramer, N. Gershenfeld, S. Swei, and K. C. Cheung, "Digital morphing wing: active wing shaping concept using composite lattice-based cellular structures," *Soft robotics*, vol. 4, no. 1, pp. 33–48, 2017.

[3] Z. Li, S. Suntharasantic, and P. Chirarattananon, "Simplified quasi-steady aeromechanic model for flapping-wing robots with passively rotating hinges," in *2018 IEEE International Conference on Robotics and Automation (ICRA)*. IEEE, 2018, pp. 1–5.

[4] P. Zhao, Q. Quan, S. Chen, D. Tang, and Z. Deng, "Experimental investigation on hover performance of a single-rotor system for mars helicopter," *Aerospace Science and Technology*, vol. 86, pp. 582–591, 2019.

[5] D. Lentink, W. B. Dickson, J. L. Van Leeuwen, and M. H. Dickinson, "Leading-edge vortices elevate lift of autorotating plant seeds," *Science*, vol. 324, no. 5933, pp. 1438–1440, 2009.

[6] K. Varshney, S. Chang, and Z. J. Wang, "The kinematics of falling maple seeds and the initial transition to a helical motion," *Nonlinearity*, vol. 25, no. 1, p. C1, 2011.

[7] W. Zhang, M. W. Mueller, and R. D'Andrea, "A controllable flying vehicle with a single moving part," in *2016 IEEE International Conference on Robotics and Automation (ICRA)*. IEEE, 2016, pp. 3275–3281.

[8] E. R. Ulrich, D. J. Pines, and J. S. Humbert, "From falling to flying: the path to powered flight of a robotic samara nano air vehicle," *Bioinspiration & biomimetics*, vol. 5, no. 4, p. 045009, 2010.

[9] J. E. Low, L. T. S. Win, D. S. B. Shaiful, C. H. Tan, G. S. Soh, and S. Foong, "Design and dynamic analysis of a transformable hovering rotorcraft (THOR)," in *2017 IEEE International Conference on Robotics and Automation (ICRA)*. IEEE, 2017, pp. 6389–6396.

[10] M. Bangura, M. Melega, R. Naldi, and R. Mahony, "Aerodynamics of rotor blades for quadrotors," *arXiv preprint arXiv:1601.00733*, 2016.

[11] P. Zhao, Q. Quan, S. Chen, T. Yang, D. Bai, D. Tang, and Z. Deng, "Geometry shape selection of naca airfoils for mars rotorcraft," *Acta Astronautica*, vol. 157, pp. 300–309, 2019.

[12] R. MacNeill and D. Verstraete, "Blade element momentum theory extended to model low reynolds number propeller performance," *The Aeronautical Journal*, vol. 121, no. 1240, pp. 835–857, 2017.

[13] M. Rwigema, "Propeller blade element momentum theory with vortex wake deflection," in *Proceedings of the 27th Congress of the International Council of the Aeronautical Sciences, Nice, France, September*, 2010, pp. 19–24.

[14] W. B. Dickson and M. H. Dickinson, "The effect of advance ratio on the aerodynamics of revolving wings," *Journal of Experimental Biology*, vol. 207, no. 24, pp. 4269–4281, 2004.

[15] Y. Lee, K. Lua, T. Lim, and K. Yeo, "A quasi-steady aerodynamic model for flapping flight with improved adaptability," *Bioinspiration & biomimetics*, vol. 11, no. 3, p. 036005, 2016.

[16] W. Hoburg and R. Tedrake, "System identification of post stall aerodynamics for UAV perching," in *AIAA Infotech@ Aerospace Conference*, 2009, p. 1930.

[17] D. Lentink and M. H. Dickinson, "Rotational accelerations stabilize leading edge vortices on revolving fly wings," *Journal of Experimental Biology*, vol. 212, no. 16, pp. 2705–2719, 2009.

[18] Y. H. Hsiao and P. Chirarattananon, "Ceiling effects for surface locomotion of small rotorcraft," in *2018 IEEE/RSJ International Conference on Intelligent Robots and Systems (IROS)*. IEEE, 2018, pp. 6214–6219.